Catalysis Science & Technology

ROYAL SOCIETY OF CHEMISTRY

PAPER

View Article Online
View Journal | View Issue

Check for updates

Cite this: *Catal. Sci. Technol.*, 2022, **12**, 1257

Tailoring graphene-supported Ru nanoparticles by functionalization with pyrene-tagged N-heterocyclic carbenes†

Adrián García-Zaragoza, ‡[a] Christian Cerezo-Navarrete, ‡[a] Andrés Mollar-Cuni,[b] Pascual Oña-Burgos, [a] Jose A. Mata, [b] Avelino Corma [a] and Luis M. Martínez-Prieto *[a]

Received 12th November 2021,
Accepted 24th December 2021

DOI: 10.1039/d1cy02063c

rsc.li/catalysis

The catalytic properties of graphene-supported ruthenium nanoparticles (Ru@rGO) have been finely tuned by modifying their metal surface with pyrene-tagged *N*-heterocyclic-carbene ligands (pyr-IMes). The nature and interaction modes of the pyr-IMes ligands on Ru@rGO were established by XPS, which were found as protonated carbenes, coordinated to the ruthenium surface and directly interacting with the graphene support. To evaluate the activity and selectivity of Ru@rGO functionalized with different equivalents of pyr-IMes (Ru@rGO/pyr-IMes$_n$; n = 0, 0.2, 0.5, 0.8 or 1), we used acetophenone hydrogenation as a model reaction. The catalytic activity and selectivity are highly dependent on the NHC surface coverage degree. The higher the amount of surface NHC ligands, the lower the activity of the catalyst, but the higher the selectivity towards 1-phenylethanol (suppressing the hydrodeoxygenation side reaction at high surface coverages). The reactivity of the most interesting catalyst, Ru@rGO/pyr-IMes$_{0.5}$, was evaluated in the hydrogenation of other molecules of interest, such as nitrobenzene, 5-hydroxymethylfurfural (HMF), quinoline or 1-methylindole, among others. Finally, by TEM analysis after catalysis we observed a clear correlation between the surface ligand coverage and the stability of the catalysts against sintering. It was then possible to control the reactivity and stability of graphene-supported Ru NPs by modifying their surface with pyr-IMes ligands.

Introduction

The catalytic use of metal nanoparticles (MNPs) for fine chemical synthesis has undergone an exponential growth since the early 90s.[1] The interest is mainly due to the particular catalytic properties of MNPs, which combine the main advantages of homogeneous and heterogeneous catalysts.[2] Generally, MNPs can be easily recycled and reused as heterogeneous catalysts, but with the characteristic high activity of the homogeneous ones. The high activity of MNPs is explained by their great number of available surface active sites due to their small size (1–100 nm) and high surface-to-volume ratio. However, this large number of surface atoms of different nature normally transforms the reactants in different ways, being difficult to precisely control the selectivity of MNPs. An efficient way to modulate the catalytic performance of MNPs is the use of organic ligands, which can modify the substrate–metal surface interactions during the catalysis and therefore change their activity and selectivity.[3] Controlling the surface chemistry of MNPs by functionalization with ancillary ligands is a well-known strategy in colloidal catalysis.[4] However, it has been much less employed in supported MNP catalysis, since traditionally it was supposed that surface ligands block active sites, decreasing the activity of the supported catalyst, which is *a priori* an undesired effect.[5] All the same, as well as in organometallic chemistry, surface ligands are also able to modify the electronic and steric properties of supported MNPs and thus, to modulate their catalytic properties.[6] Thus, the better stability/recyclability of supported MNPs compared to those of colloidal MNPs, together with the possibility of controlling the activity/selectivity through their surface modification with organic ligands, make functionalized supported MNPs promising catalysts for industrial processes, since they combine all the benefits of heterogeneous (stability and recyclability) and homogeneous (activity and selectivity) catalysis.

---

[a] *ITQ, Instituto de Tecnología Química, Universitat Politècnica de València-Consejo Superior de Investigaciones Científicas, Av. de los Naranjos S/N 46022, Valencia, Spain. E-mail: luismiguel.martinez@csic.es*

[b] *Institute of Advanced Materials (INAM), Universitat Jaume I, Avda. Sos Baynat S/N 12006, Castellón, Spain*

† Electronic supplementary information (ESI) available. See DOI: 10.1039/d1cy02063c

‡ These authors contributed equally to this work.

Selective supported metal catalysts are highly important in the industrial synthesis of chemicals.[7] Most industrial catalysts are MNPs supported on high surface area materials that maximize the metal surface exposure.[8] A strong interaction between the MNPs and the support is crucial to obtain stable catalysts. Moreover, the reactivity of supported MNPs will not only depend on the particular electronic properties of the metal sites, but also on the chosen support, which, as well as surface ligands, can modify their reactivity.[9] Therefore, the selection of an appropriate support with suitable properties (thermal stability, high surface area, basic/acidic sites, *etc.*) is fundamental for the stabilization of MNPs and to control their catalytic properties. In this line, high surface area two-dimensional (2D) structures such as reduced graphene oxide (rGO) are appealing supports for MNPs due to their specific electronic configuration that results in strong MNP–graphene interactions.[10] As already mentioned, these metal–graphene interactions can also modify the electronic properties of the supported MNPs, changing their reactivity.[11] In addition, the defect sites normally present in rGO are excellent anchoring points for MNPs, facilitating their generation and stabilization.[12] All this, together with the recent advances in the synthesis of graphene materials, makes graphene-supported MNPs attractive heterogeneous catalysts for industrial applications.

Since the isolation of the first example of an *N*-heterocyclic carbene (NHC),[13] this type of compound has been extensively used as an ancillary ligand in coordination chemistry.[14] Due to their excellent electron donating properties, NHC ligands strongly coordinate to transition metals, being exceptional ligands for transition metal complexes.[15] However, they are not only suitable ligands for the stabilization of organometallic complexes, but also effective MNP stabilizers.[16] Indeed, during the last decade a great number of NHC-stabilized MNPs have been reported, including Au,[17] Ir,[18] Ru,[19] Ni,[20] Pd,[21] or Pt[22] NPs. Moreover, NHCs have been demonstrated to be an efficient tool to modify the size, stability, solubility and catalytic properties of MNPs. Depending on the molecular structure (*e.g.* backbone with long alkyl chains) or *N*-substituents (*e.g.* bulky groups) of the stabilizing NHC, the resulting MNPs will display different properties.[16,23] Thanks to their versatility, NHC-stabilized MNPs have been successfully applied in numerous catalytic processes such as hydroboration,[24] oxidation,[23c] deuteration[25] and hydrogenation reactions.[26] In the same way that NHCs can modify the catalytic properties of colloidal MNPs, they can be also used to functionalize supported MNPs and thereby modulate their surface chemistry.[27] For example, in 2016, Glorius *et al.* reported how to control the selectivity of Ru/K–Al_2O_3 by functionalization with NHCs in the hydrogenation of phenylacetylene to ethylbenzene.[28] Pieters *et al.* also controlled the selectivity of Ru NPs supported on carbon in the isotopic H/D exchange by modifying the surface metal with NHCs.[29] However, the surface modification of supported MNPs with NHCs not only may improve their selectivity, but also is able to increase their stability. Recently, it has been shown that NHCs bearing a pyrene group can enhance the stability of graphene-supported MNPs *via* non-covalent π-interactions between the pyrene tag and the graphene layer.[30]

Herein, we present Ru NPs supported on reduced graphene oxide (**Ru@rGO**) functionalized with different equivalents (0.2, 0.5, 0.8 and 1 equiv.) of an NHC ligand containing a pyrene group (pyr-IMes). The obtained catalytic systems (**Ru@rGO/pyr-IMes**) have been fully characterized by state-of-the-art techniques. Additionally, it has been possible to modify their stability, activity and selectivity in the hydrogenation of different substrates (*i.e.* acetophenone, decanal, nitrobenzene, styrene, 3-methyl-2-cyclohexenone, quinoline, 1-methylindole and HMF) by means of the NHC surface coverage.

Results and discussion

Synthesis, characterization and surface studies

Ruthenium nanoparticles supported on rGO (**Ru@rGO**) functionalized with NHC ligands containing a pyrene tag were prepared by following a two-step synthetic route (Fig. 1). First, (i) Ru NPs were generated through an organometallic approach and directly immobilized onto reduced graphene oxide (rGO). More specifically, graphene supported Ru NPs (**Ru@rGO**) were generated by the controlled decomposition of Ru(COD)(COT) (COD: cyclooctadiene; COT: cyclooctatriene) under 3 bar H_2 in a THF dispersion of rGO, according to a previously reported procedure.[31] Then, (ii) the as-synthesized **Ru@rGO** was functionalized with different amounts of a pyrene-tagged *N*-heterocyclic carbene ligand (n = 0.2, 0.5, 0.8 or 1 equivalent relative to ruthenium),[32] formed by the deprotonation of the corresponding imidazolium salt with K^tBuO. Purification by washing with THF yields Ru NPs immobilized onto rGO functionalized with NHC ligands as black powders, namely **Ru@rGO/pyr-IMes$_n$**.

Ruthenium contents in **Ru@rGO** and **Ru@rGO/pyr-IMes$_n$** were determined by inductively coupled plasma optical emission spectroscopy (ICP-OES) analysis employing an optimized digestion method.[31] In all cases, the ruthenium content was close to the theoretical value of 3 wt% (for more details see the Experimental section).

Transmission electron microscopy (TEM) analysis of the unmodified **Ru@rGO** revealed the presence of small spherical Ru NPs displaying low dispersion in size, good distribution on the graphene support and a mean diameter of 1.5 ± 0.5 nm (Fig. 2a). After their functionalization with 0.2, 0.5, 0.8 or 1 equivalent (equiv.) of pyr-IMes (**Ru@rGO/pyr-IMes$_n$**), the morphology, size, dispersion and distribution of the graphene-supported Ru NPs did not significantly change (Fig. 2b; see the ESI,† Fig. S1–S3). A high-resolution TEM (HRTEM) micrograph of **Ru@rGO** (Fig. S4†) shows the presence of crystalline nanoparticles with a hexagonal close-packed (hcp) structure characteristic of bulk Ru(0). The Fourier transform analysis applied to this picture shows reflection planes at (102), (002) and (101).

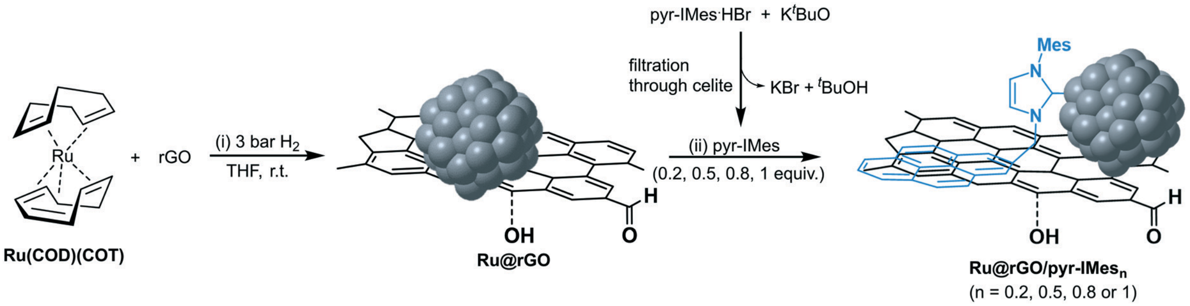

Fig. 1 Two-step synthetic route followed for the synthesis and subsequent functionalization of **Ru@rGO** with pyr-IMes.

Since Raman spectroscopy is an established technique to investigate the quality of graphenic materials (defects, exfoliation degree, sp^2 character, *etc.*), **rGO**, **Ru@rGO** and **Ru@rGO/pyr-IMes$_{0.5}$** were analyzed by this spectroscopic technique. In all recorded Raman spectra, two well-differenced domains were observed, one located between 1200 and 1700 cm^{-1} and another one from 2500 to 3250 cm^{-1} (see the ESI,† Fig. S5–S7). The first domain contains two bands of similar intensities at 1354 and 1595 cm^{-1}, which correspond to D and G bands, respectively. A high ratio of the intensities of these bands (I_D/I_G) is related to a high percentage of defect sites, which are normally excellent anchoring points for MNP stabilization.[12,33] In addition, comparing the I_D/I_G ratios before (rGO; Fig. S5†) and after the incorporation of Ru NPs (**Ru@rGO** or **Ru@rGO/pyr-IMes$_{0.5}$**; Fig. S6 and S7†), a slight decrease from 1.54 to 1.50 was observed. This decrease in the I_D/I_G ratio is an indication of the increase of the sp^2 character of **Ru@rGO** and **Ru@rGO/pyr-IMes$_{0.5}$**, mainly due to the incorporation of Ru NPs. The second domain centered at *ca.* 3000 cm^{-1} corresponds to the 2D band and is related to a few graphene layers.

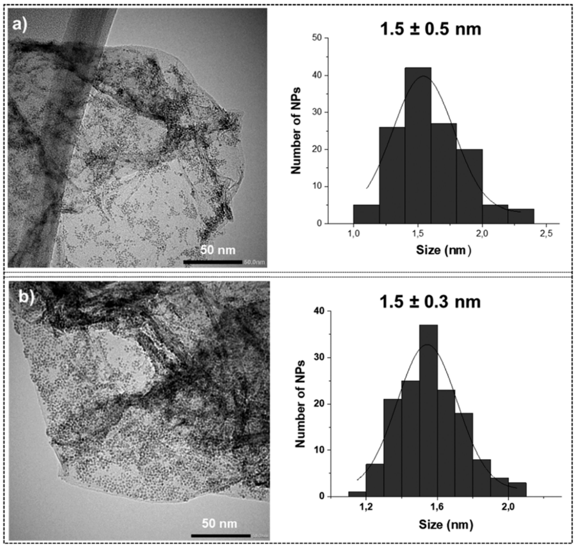

Fig. 2 Comparative TEM images and size distribution histograms of (a) **Ru@rGO** and (b) **Ru@rGO/pyr-IMes$_{0.5}$**.

A series of surface studies were performed in order to better understand the coordination mode, location and dynamics of the pyrene-tagged *N*-heterocyclic carbenes at the MNP surface. First, to estimate the precise amount of pyr-IMes ligand incorporated into each one of the functionalized catalysts, a combined study involving elemental analysis (EA) and BET surface area determination was carried out. Once the available surface area of **Ru@rGO** was determined (331.8 m^2 g^{-1}), we calculated by EA the real amount of pyr-IMes ligand added onto **rGO** and thus, the actual number of equivalents of pyrene-tagged NHCs with which each catalyst has been functionalized (Table S1†). As a general trend, only half of the amount of NHC ligand added during the synthesis was finally incorporated into the functionalized catalysts.

Subsequently, a CO chemisorption analysis was performed to determine the accessible ruthenium surface of the unmodified **Ru@rGO** and the functionalized **Ru@rGO/pyr-IMes$_{0.5}$** and therefore, to evidence the coordination of the carbene ligand to the ruthenium surface. For the unmodified **Ru@rGO**, the CO uptake was 62.1 μg g^{-1}, while for **Ru@rGO/pyr-IMes$_{0.5}$**, the uptake of CO decreased to 35.9 μg g^{-1}. The decrease in the number of available Ru sites on **Ru@rGO/pyr-IMes$_{0.5}$** is attributed to the coordination of pyr-IMes onto the Ru surface, which blocks the potential CO adsorption sites. Therefore, this partial decrease in the chemisorption of CO not only confirms the coordination of pyr-IMes to Ru NPs, but also demonstrates the presence of available active surface sites on the functionalized catalysts. With the aim of shedding some light on the nature and location of these active sites and to further investigate the coordination of pyr-IMes at the Ru surface, the unmodified and functionalized graphene-supported Ru NPs were studied by IR and solid-state MAS-NMR spectroscopy using CO as a probe molecule. However, due to their opacity and conductivity (which made the tuning of the NMR probe impossible), these analyses were unsuccessful. To circumvent this limitation, colloidal/unsupported Ru NPs stabilized with 0.2 and 0.5 equiv. of pyr-IMes (**Ru/pyr-IMes$_{0.2}$** and **Ru/pyr-IMes$_{0.5}$**) were synthesized and fully characterized, including IR and MAS-NMR surface studies using CO as molecular probe. NHC ligand-stabilized Ru NPs were prepared by following the same organometallic approach shown in Fig. 1, but using the pyrene-tagged NHC ligands as a stabilizer (Fig. 3). Here, the

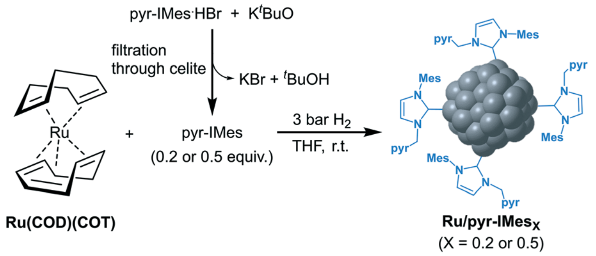

Fig. 3 Synthesis of ligand-stabilized **Ru/pyr-IMes** NPs following the organometallic approach.

non-supported Ru NPs are directly stabilized by the NHC ligands, as has been previously described.[23b]

The TEM and HRTEM images of **Ru/pyr-IMes$_{0.2}$** and **Ru/pyr-IMes$_{0.5}$** showed small, crystalline and monodispersed Ru NPs with a mean diameter of 1.4 ± 0.4 and 1.3 ± 0.4 nm, respectively (see the ESI,† Fig. S8–S10). The ICP analyses of **Ru/pyr-IMes$_{0.2}$** and **Ru/pyr-IMes$_{0.5}$** gave ruthenium contents of 55.7 and 33.2 wt%, respectively. It is worth mentioning that the ratio between the surface ruthenium atoms and coordinated NHC ligands ($Ru_{(s)x}/L_y$) is not large enough to accommodate all the ligands on the Ru surface (steric hindrance). More specifically, **Ru/pyr-IMes$_{0.2}$** exhibits a $Ru_{(s)x}/L_y$ ratio of *ca.* 4.1, while the ratio for **Ru/pyr-IMes$_{0.5}$** is even lower, 1.4 (see the ESI,† Table S2). Therefore, we can assume that the remaining surface ligands are organized in a second coordination sphere by π–π stacking between the aromatic side groups of the pyrene-tagged NHCs. This type of second sphere of non-coordinated ligands has been previously observed in similar ligand-stabilized MNPs.[22,34]

Afterwards, the surface state of **Ru/pyr-IMes$_{0.2}$** and **Ru/pyr-IMes$_{0.5}$** was investigated by evaluating their capacity to bind CO by diffuse reflectance infrared Fourier transform (DRIFT) and $^{13}C\{^1H\}$ MAS NMR with ^1H–^{13}C cross-polarization (CP). Here the aim was to locate the available surface active sites of these NHC-stabilized Ru NPs. Fig. S11 and S12 (see the ESI†) show the DRIFT spectra of **Ru/pyr-IMes$_{0.2}$** and **Ru/pyr-IMes$_{0.5}$** before (blue) and after (red) exposure to CO (bubbling CO in a THF solution, for more details see the Experimental section). Interestingly, before the reaction with CO, both spectra already exhibited a weak and broad band at *ca.* 1900 cm^{-1}, corresponding to adsorbed CO. The presence of this band is attributed to the decarbonylation of THF during the synthesis of the nanoparticles, as previously observed.[23c,35] After the reaction with CO, both spectra showed an increase in intensity and a shift to higher frequency (*ca.* 2000 cm^{-1}) of the aforementioned band. This confirmed the coordination of CO and the high availability of free Ru active sites at the NP surface, even in the presence of a large number of surface NHC ligands, as was previously determined by ICP (see the ESI,† Table S2).

The $^{13}C\{^1H\}$ CP-MAS NMR spectrum of **Ru/pyr-IMes$_{0.2}$** showed a number of distinct peaks characteristic of the pyrene-tagged NHC ligand (see the ESI,† Fig. S13a). The broad signal at *ca.* 130 ppm was assigned to the aromatic rings of the mesitylene and pyrene groups, together with the imidazole backbone. The peaks between 50 and 10 ppm were attributed to the CH_2 group connected to the pyrene tag, as well as the methyl groups of the N-bonded mesitylene. After exposure of **Ru/pyr-IMes$_{0.2}$** NPs to 1 bar ^{13}CO at room temperature (r.t.), the $^{13}C\{^1H\}$ CP-MAS NMR spectrum showed two new signals ascribed to adsorbed CO (Fig. S13b†). The broad and low-intensity resonance at *ca.* 230 ppm corresponds to ^{13}CO coordinated in a bridging mode (CO_b), and the sharp and intense peak at *ca.* 200 ppm is due to ^{13}CO adsorbed in a terminal mode (CO_t). It is well known that bridging CO molecules coordinate onto faces (or terraces) of nanoparticles and terminal ones onto their apexes and edges.[36] Since most of the CO coordinates in a terminal mode, we can assume that the ruthenium faces are not accessible due to the π interactions between the aromatic rings of the pyrene and the ruthenium terraces, which hinders the coordination of CO in a bridging mode.[37] Furthermore, the appearance of spinning sidebands (*) suggests that the terminal CO molecules are static on the surface. This lack of mobility of CO_t on the ruthenium surface can be explained by the coordination of NHC ligands near the active sites where CO molecules are adsorbed. The $^{13}C\{^1H\}$ CP-MAS NMR spectrum of **Ru/pyr-IMes$_{0.5}$** after exposure to ^{13}CO showed similar resonances, but with a new peak at 204 ppm (see the ESI,† Fig. S14). This new resonance may correspond to the CO coordinated in a multi-terminal mode, as previously reported for Rh NPs.[38] Again, we observed by CP-MAS NMR a great number of free active sites on these non-supported Ru NPs even at high surface ligand coverages.

The coordination of pyr-IMes onto the non-supported **Ru/pyr-IMes$_{0.5}$** NPs was also investigated by X-ray photoelectron spectroscopy (XPS), since it is a useful technique to study the binding mode of NHC surface ligands on MNPs.[39] The N 1s area of **Ru/pyr-IMes$_{0.5}$** presents a binding energy (BE) of 399.1 eV (Fig. 4a, orange), which is shifted to low BE values compared to that of the corresponding imidazolium salt **pyr-IMes·HBr** (400.9 eV) (Fig. 4a, green). This decrease in the BE is due to a loss of electron density of the N atoms of pyr-IMes and indicates the direct coordination of the NHC ligand to the ruthenium surface. XPS analysis was also employed to investigate the coordination of the pyrene-tagged NHC ligand onto the graphene-supported Ru NPs functionalized with 0.5 equivalents of pyr-IMes (**Ru@rGO/pyr-IMes$_{0.5}$**). For **Ru@rGO/pyr-IMes$_{0.5}$** the N 1s peak is centered at 399.6 eV and can be deconvoluted into three contributions with different BEs (Fig. 4b), corresponding to pyr-IMes coordinated to Ru (398.9 eV), interacting with rGO (399.8 eV), and protonated (401.2 eV). To confirm the BE of pyr-IMes which directly interacts with the rGO support (**rGO/pyr-IMes**), most probably by π-interactions between the pyrene tags of the NHC and the graphene layer, free NHC was added to a dispersion of rGO in THF and analyzed by XPS (for more details see the Experimental section). And, as was expected, the N 1s signal of **rGO/pyr-IMes** revealed a peak at 399.8 eV, which is located

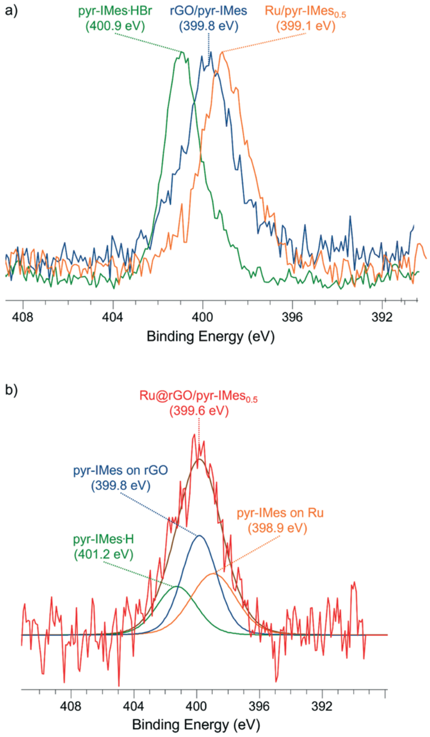

Fig. 4 X-ray photoelectron spectroscopy (XPS) spectra of (a) the N 1s signals of pyr-IMes·HBr (green), **rGO/pyr-IMes** (blue), **Ru/pyr-IMes$_{0.5}$** (orange) and (b) **Ru@rGO/pyr-IMes$_{0.5}$** (red).

between the N 1s peaks of the corresponding imidazolium salt and the pyr-IMes ligand coordinated to ruthenium (Fig. 4a, blue). Therefore, using XPS we were able to evaluate the different nature and chemical environments of pyr-IMes ligands on the functionalized catalyst, **Ru@rGO/pyr-IMes$_{0.5}$**: (i) protonated (400.9 eV), (ii) coordinated to ruthenium (399.1 eV) and (iii) interacting with the graphene support (399.8 eV) (Fig. 4). Furthermore, by analyzing their N 1s XPS areas after deconvolution, we can deduce that approximately 32% of the NHC ligand is coordinated to Ru, 45% interacts with the graphene support and 23% is protonated.

Moreover, the oxidation state of the ruthenium was also investigated by XPS upon analyzing the Ru 3p region of **Ru/pyr-IMes$_{0.5}$**, **Ru@rGO** and **Ru@rGO/pyr-IMes$_{0.5}$** (Fig. S15†). The Ru 3p$_{3/2}$ signal of the ligand-stabilized **Ru/pyr-IMes$_{0.5}$** was found at 462.2 eV, which after deconvolution showed two contributions, a main contribution at *ca.* 461.4 eV, attributed to Ru(0), and a minor one at *ca.* 463.8 eV, corresponding to RuO_2 (Fig. S15a†). On the other hand, the Ru 3p$_{3/2}$ signals of graphene-supported Ru NPs unmodified and modified with pyr-IMes were observed at 463.1 and 463.4 eV, respectively (see the ESI,† Fig. S15b and c). After deconvolution, we observed that most of the ruthenium was oxidized to Ru(IV). This is mainly due to the purification process of the graphene-supported Ru NPs, which is carried out in air (see the Experimental section). For this reason, a preliminary activation step (1 h at 150 °C and 50 bar H_2) was necessary before catalysis. This activation step reduces most of the RuO_2 to Ru(0), which is the active species in hydrogenation reactions.

Catalytic studies

First, to evaluate the influence of the pyrene-tagged NHC ligands on the activity and selectivity of the graphene-supported Ru NPs, the hydrogenation of acetophenone was used as a model reaction. This substrate is an interesting model molecule since it contains two potentially reducible functional groups (*i.e.* a ketone and a phenyl group), and the activity/selectivity of the functionalized catalysts herein prepared can be simply compared. Acetophenone (**1**) can be reduced to 1-cyclohexylethanol (**4**) through two pathways: (i) *via* 1-phenylethanol (**2**), hydrogenating first the ketone, and (ii) *via* 1-cyclohexylethanone (**3**), where the phenyl group is hydrogenated before (top of Table 1). Additionally, ethylbenzene (**5**) and ethylcyclohexane (**6**) can be also formed by hydrodeoxygenation (HDO) processes. By checking the selectivity of the non-functionalized **Ru@rGO** at total conversion (20 h, Table 1, entry 1), it can be seen that it mostly produces the over reduced product **4** (81.5%) together with **6** (18.5%), which comes from HDO processes. After 20 h reaction, **Ru@rGO/pyr-IMes$_{0.2}$** also shows complete conversion and a considerable amount of HDO products **5** (3.9%) and **6** (16.7%), but with a lower selectivity towards **4** (69.6%). Comparing the initial reaction rates of **Ru@rGO** and **Ru@rGO/pyr-IMes$_{0.2}$** (Fig. 5a and b), the unmodified Ru NPs show the highest activity. After 1 hour of reaction, **Ru@rGO** exhibits an acetophenone conversion of 98%, while the conversion by using **Ru@rGO/pyr-IMes$_{0.2}$** as catalyst is only 56%. The initial reaction rate for **Ru@rGO/pyr-IMes$_{0.5}$** slightly decreases in comparison to that for **Ru@rGO/pyr-IMes$_{0.2}$** (Fig. 5b and c); however, it was accompanied with an increase of the selectivity towards the fully hydrogenated product **4** and a significant drop in the formation of HDO products. More specifically, after 20 h, a conversion of *ca.* 98.6% was achieved with a selectivity towards **4** of 84.1%, producing only 8.9% of **6** (Table 1, entry 3). Upon increasing the number of equivalents of pyr-IMes up to 0.8 (**Ru@rGO/pyr-IMes$_{0.8}$**), we find a marked decrease in the activity, together with a substantial increase in the selectivity towards **2**, giving after 20 h reaction 63.6% 1-phenylethanol at 95.9% conversion (Fig. 5d; Table 1, entry 4). Finally, the graphene-supported Ru NPs with the highest surface coverage, **Ru@rGO/pyr-IMes$_1$**, displays the lowest activity, but the highest selectivity towards **2** (98% selectivity at 60.2% conversion), practically avoiding the formation of HDO products (Fig. 5e; Table 1, entry 5). These results show a clear correlation between the surface coverage degree and the activity and selectivity of the functionalized catalysts. The higher the amount of surface pyr-IMes ligands, the lower the activity of the catalyst, but the higher the selectivity towards **2**. In addition, at higher surface coverages the formation of HDO products is avoided. Both the decrease in the activity and the selectivity improvement can be explained by the blockage of the ruthenium active

Table 1 Hydrogenation of acetophenone catalyzed by **Ru@rGO/pyr-IMes$_n$** (X = 0.2, 0.5, 0.8 or 1) and **Ru@rGO/ICy$_1$**[a]

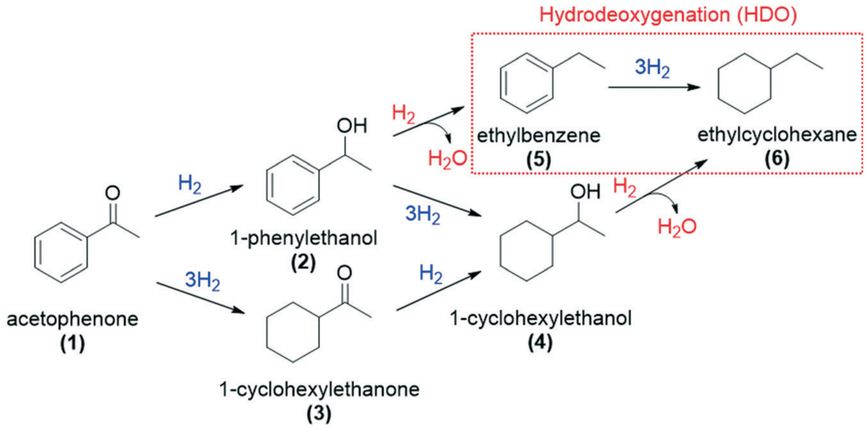

Entry	Catalyst	Conversion[b,c] (%)	Selectivity[b] (%)				
			2	3	4	5	6
1	**Ru@rGO**	>99	0.0	0.0	81.5	0.0	18.5
2	**Ru@rGO/pyr-IMes$_{0.2}$**	>99	1.1	8.7	69.6	3.9	16.7
3	**Ru@rGO/pyr-IMes$_{0.5}$**	98.6	1.9	5.0	84.1	0.1	8.9
4	**Ru@rGO/pyr-IMes$_{0.8}$**	95.9	63.6	9.8	21.7	4.2	0.7
5	**Ru@rGO/pyr-IMes$_1$**	60.2	98.0	0.8	0.6	0.6	0.0
6	**Ru@rGO/ICy$_1$**	98.4	0.0	9.6	77.2	3.7	9.5

[a] Reaction conditions: 0.5 mmol acetophenone, 0.5 mol% cat (0.0025 mmol Ru), 10 mL THF, 50 bar H_2, 130 °C, 20 h. [b] Conversions and selectivities were determined by GC using dodecane as the internal standard and confirmed by GC-MS. [c] Metal-free rGO exhibited negligible activity in the hydrogenation of acetophenone under these reaction conditions.

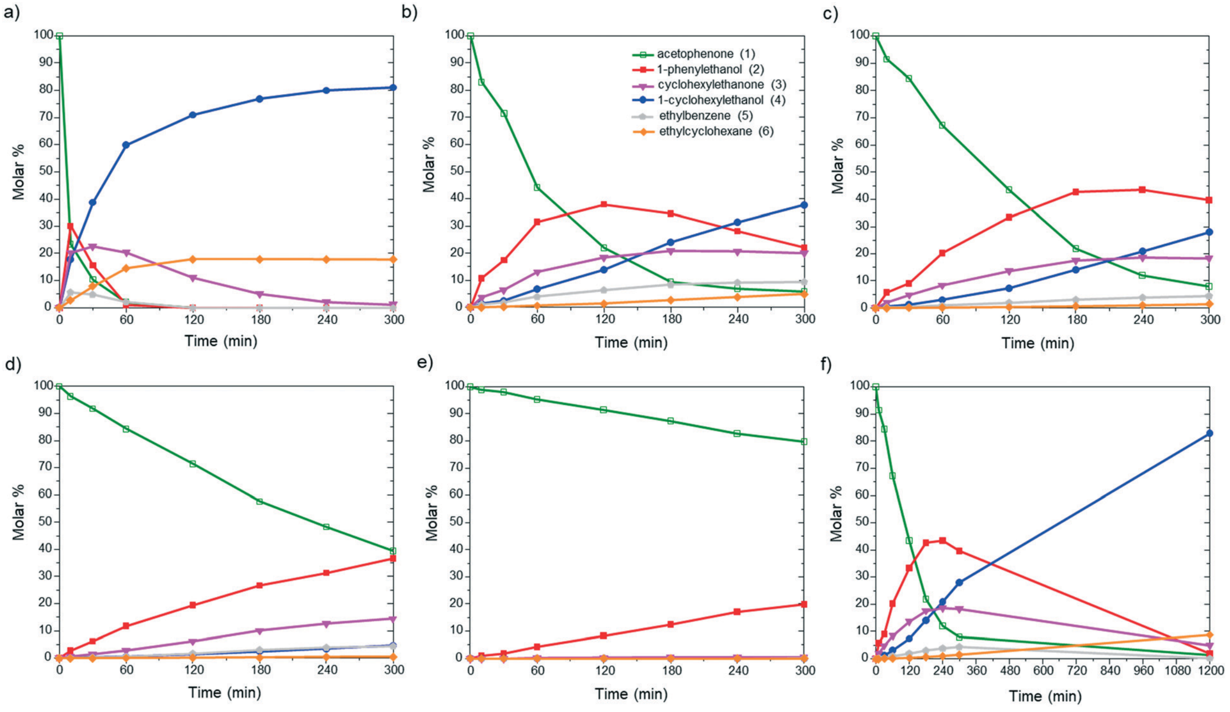

Fig. 5 Hydrogenation of acetophenone using (a) **Ru@rGO**, (b) **Ru@rGO/pyr-IMes$_{0.2}$**, (c and f) **Ru@rGO/pyr-IMes$_{0.5}$**, (d) **Ru@rGO/pyr-IMes$_{0.8}$**, and (e) **Ru@rGO/pyr-IMes$_1$** as catalysts.

sites by pyr-IMes ligands. As we increase the number of equivalents of pyr-IMes, the amount of free ruthenium sites decreases, and therefore, the activity is negatively affected. However, this blockage of active sites also improves the selectivity of the functionalized catalysts, not only avoiding the undesired HDO side reactions (*i.e.* **Ru@rGO/pyr-IMes$_{0.5}$**;

Table 1, entry 3), but also hydrogenating selectively acetophenone to 1-phenylethanol at high surface coverages (*i.e.* **Ru@rGO/pyr-IMes$_1$**; Table 1, entry 5). It is important to mention that the selective hydrogenation of aromatic ketones to form benzyl alcohols is normally catalyzed by homogeneous catalysts,[40] since heterogeneous catalysts generally produce mixtures of **2**, **3** and **4**.[41] Altogether, these findings demonstrate that it is possible to control the selectivity of graphene-supported Ru NPs during acetophenone hydrogenation by modifying their metal surface with pyrene-tagged N-heterocyclic carbene ligands.

Among all the catalytic systems studied in the acetophenone hydrogenation reaction, **Ru@rGO/pyr-IMes$_{0.5}$** is the most attractive one since it presents the best compromise between activity and selectivity. This functionalized catalyst hydrogenates selectively acetophenone to 1-cyclohexylethanol, minimizing the generation of HDO products (Fig. 5f; Table 1, entry 3). Therefore, **Ru@rGO/pyr-IMes$_{0.5}$** was also tested in the hydrogenation of various substrates that contain other reducible functional groups such as aldehyde, vinyl, heterocyclic or nitro groups, under the same catalytic conditions (Table 2). Decanal (**7**) was selectively hydrogenated to 1-decanol (**8**) after 5 h reaction, without formation of the HDO product **9** (Table 2, entry 1). After 2 h, nitrobenzene (**10**) was also selectively converted to cyclohexylamine (**12**) (Table 2, entry 2). Similar reactivity was observed in the hydrogenation of 3-methyl-2-cyclohexenone (**13**) and quinoline (**16**). Both substrates, after 5 h, gave full conversion with high selectivity towards the corresponding over reduced product (Table 2, entries 3 and 4). On the other hand, at the same reaction time, styrene (**20**) only produced 43% ethylcyclohexane (**22**). Furthermore, we investigated the catalytic activity of **Ru@rGO/pyr-IMes$_{0.5}$** in other molecules of current interest such as 1-methylindole (**23**), which can be used as a liquid hydrogen carrier (LOHC), or 5-(hydroxymethyl)furfural (HMF; **27**), a platform molecule derived from biomass. After 5 h reaction, **Ru@rGO/pyr-IMes$_{0.5}$** presented a 96% conversion of **23** with 90% selectivity towards the completely hydrogenated product 1-methyl-octahydroindole (**22**) (Table 2, entry 6). At longer reaction times (20 h), a complete conversion with 100% selectivity to **22** was achieved (Table 2, entry 7).These results are of high interest for hydrogen storage applications, since 1-methylindole is a promising LOHC due to its low melting

Table 2 Hydrogenation reactions catalyzed by **Ru@rGO/pyr-IMes$_{0.5}$**[a]

Entry	Substrates	Products	Time (h)	Conversion[b] (%)	Selectivity[b] (%)
1	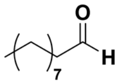 (**7**)	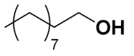 (**8**) + 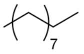 (**9**)	5	>99	**8 : 9** = 100 : 0
2	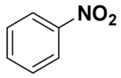 (**10**)	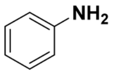 (**11**) + 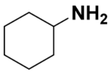 (**12**)	2	>99	**11 : 12** = 0 : 100
3	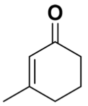 (**13**)	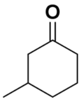 (**14**) + 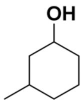 (**15**)	5	>99	**14 : 15** = 4 : 96
4	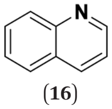 (**16**)	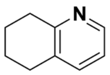 (**17**) + 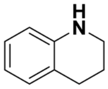 (**18**) + 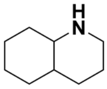 (**19**)	5	>99	**17 : 18 : 19** = 0 : 9 : 91
5	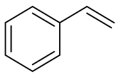 (**20**)	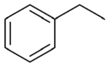 (**21**) + 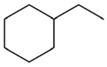 (**22**)	5	>99	**21 : 22** = 57 : 43
6	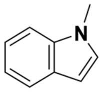 (**23**)	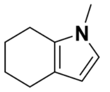 (**24**) + 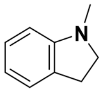 (**25**) + 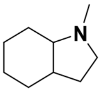 (**26**)	5	96	**24 : 25 : 26** = 9 : 1 : 90
7			20	>99	**24 : 25 : 26** = 0 : 0 : 100
8	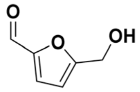 (**27**)	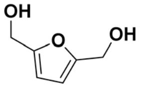 (**28**) + 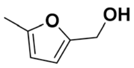 (**29**) + 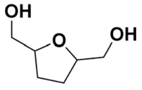 (**30**)	5	>99	**28 : 29 : 30** = 92 : 2 : 6

[a] Reaction conditions: 0.5 mmol substrates, 0.5 mol% cat (0.0025 mmol Ru), 10 mL THF, 50 bar H_2, 130 °C. [b] Conversions and selectivities were determined by GC using dodecane as the internal standard and confirmed by GC-MS.

point (−20 °C) and high hydrogen content (5.76 wt%).[42] Due to the great potential of this functionalized catalyst, **Ru@rGO/pyr-IMes$_{0.5}$** has been also tested in the hydrogenation of an interesting biomass derived platform molecule, *i.e.* HMF (**27**). After 5 h of reaction, **Ru@rGO/pyr-IMes$_{0.5}$** showed a quantitative conversion with excellent selectivity towards 5-bis(hydroxymethyl)furan (BHMF) (**28**) (92%, Table 2, entry 8). HDO and hydrogenation products **29** and **30** were also formed, but in minute amounts.

A series of experiments were performed to investigate the influence of the surface pyrene-tagged NHCs on the stability of graphene-supported Ru NPs. First, we analyzed by TEM the size and morphology of Ru NPs present on the unmodified and modified catalytic systems after a standard catalytic test (hydrogenation of acetophenone for 20 h at 50 bar H_2 and 130 °C). The Ru NPs supported on **Ru@rGO** significantly increased their size from 1.5 to 2.3 nm (Table 3, entry 1). On the other hand, Ru NPs on **Ru@rGO/pyr-IMes$_1$** practically did not increase in size after catalysis (from 1.6 to 1.7 nm; Table 3, entry 5). The analysis after catalysis of the Ru NPs immobilized on the other three functionalized catalytic systems showed intermediate sizes. More specifically, we observed that the main diameter of the nanoparticles after catalysis decreases as the number of equivalents of pyr-IMes in the system increases (Table 3, entries 2–4). Therefore, there is an evident correlation between the amount of surface NHC ligands and the stability of the supported Ru NPs against sintering (Fig. S16–S20). The higher the surface coverage, the more resistant the catalyst is to sintering. This demonstrates the ability of the pyr-IMes ligands to increase the stability of graphene-supported MNPs, as previously reported for similar systems.[30]

The influence of the pyrene tag on the activity/selectivity and stability of **Ru@rGO/pyr-IMes** was evaluated by using as a modifier another NHC ligand without polyaromatic groups on the *N*-substituents. Concretely, **Ru@rGO** was functionalized with 1 equiv. of an NHC with cyclohexyl groups on the *N*-substituents (1,3-dicyclohexylimidazol-2-ylidene; ICy) following the two-step synthetic route in Fig. 1 (**Ru@rGO/ICy$_1$**) (Fig. S21†). In this case, the absence of the pyrene tag affected both the selectivity and stability of the resulting catalyst. After studying the reactivity of **Ru@rGO/ICy$_1$** during the hydrogenation of acetophenone, we observed that it was not possible to control the selectivity of the catalyst in the same way as with **Ru@rGO/pyr-IMes$_1$** (Fig. S22†). Here, even at high NHC surface coverage (1 equiv. of ICy), we observed the hydrogenation of both functional groups (carbonyl and phenyl), with the totally hydrogenated product **4** being the main product after 20 h (Table 1, entry 6). Probably, the lack of aromatic groups of ICy allows the interaction between the acetophenone and the faces of the Ru NPs and thus, the hydrogenation of phenyl groups. Already reported surface studies on colloidal Ru nanoparticles stabilized by ICy confirm the presence of free available faces.[23b] Contrary to the pyr-IMes ligands, which through π-interactions block the ruthenium terraces of **Ru@rGO/pyr-IMes$_1$**, and make it highly selective in the hydrogenation of acetophenone (**1**) to 1-phenylethanol (**2**). The surface modification of **Ru@rGO** with ICy neither controls the formation of HDO side-products **5** and **6.** By analyzing the size of Ru NPs present on **Ru@rGO/ICy$_1$** before and after the standard catalytic test (hydrogenation of acetophenone) by TEM (Table 3, entry 6; Fig. S23 and S24†), we observed a noticeable increase in size, from 1.5 to 2.3 nm, similar to that observed in the unmodified **Ru@rGO**. In addition, the nanoparticle distribution observed after catalysis is much less uniform (Fig. S24†). The absence of π-interactions between the ICy ligands and the graphene layer explains the lower stability of these Ru NPs against sintering. Altogether, these results highlight the importance of the presence of the pyrene tag in the NHC used as a modifier to control the selectivity and the stability of these functionalized catalysts.

Table 3 Mean diameter of graphene-supported Ru NPs before and after catalysis

Entry	Catalyst	Size before catalysis (nm)	Size after catalysis (nm)
1	**Ru@rGO**	1.5 ± 0.5	2.3 ± 0.5
2	**Ru@rGO/pyr-IMes$_{0.2}$**	1.5 ± 0.4	2.1 ± 0.5
3	**Ru@rGO/pyr-IMes$_{0.5}$**	1.5 ± 0.3	1.9 ± 0.3
4	**Ru@rGO/pyr-IMes$_{0.8}$**	1.5 ± 0.7	1.8 ± 0.4
5	**Ru@rGO/pyr-IMes$_1$**	1.5 ± 0.4	1.7 ± 0.4
6	**Ru@rGO/ICy$_1$**	1.6 ± 0.5	2.3 ± 0.5

To test the recyclability of **Ru@rGO/pyr-IMes$_{0.5}$** a multi-addition experiment was performed. Specifically, the hydrogenation of acetophenone was carried out during seven consecutive additions of the substrate (every 12 h) using **Ru@rGO/pyr-IMes$_{0.5}$** as a catalyst. Interestingly, we observed that the catalyst not only retained the activity during this multi-addition experiment, but also improved the selectivity to 1-cyclohexyletanol (**4**) (Fig. 6). This progressive increase in the reactivity during the first addition cycles is explained by the formation of a more active surface under catalytic conditions, due to the gradual reduction of the Ru metal surface (which is partially oxidized in the as-synthesized Ru

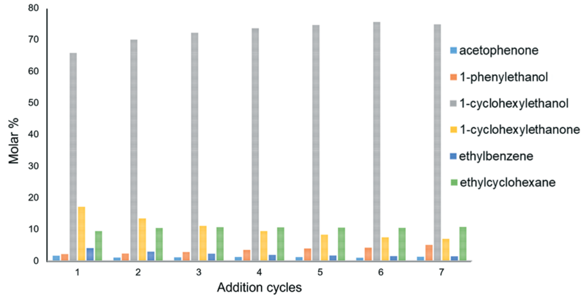

Fig. 6 Multi-addition experiment for the hydrogenation of acetophenone catalyzed by **Ru@rGO/pyr-IMes$_{0.5}$**. Conditions: Acetophenone (0.5 mmol), 0.5 mol% cat (0.0025 mmol metal), THF, 50 bar H_2, 130 °C, 12 h. Every 12 hours, acetophenone (0.5 mmol) was added to the reaction mixture. Conversions and selectivities were determined by GC using dodecane as the internal standard and confirmed by GC-MS.

NPs as was observed by XPS). The TEM analysis of **Ru@rGO-pyr-IMes$_{0.5}$** after the multi-addition experiment revealed Ru NPs similar in size and distribution to the as-prepared ones (Fig. S25†). These results underline the high stability of this functionalized catalyst under catalytic conditions during long reaction times (up to 86 h).

Finally, to verify the heterogeneous nature of **Ru@rGO/pyr-IMes$_{0.5}$**, a "hot filtration" experiment was performed during the hydrogenation reaction of acetophenone (130 °C, 50 bar H_2). After 2 h reaction, the solid **Ru@rGO/pyr-IMes$_{0.5}$** was separated by thermal filtration and the mother liquor solution was transferred to an empty reactor and then pressurized and heated. No change in the conversion was observed after 4 hours under the same catalytic conditions. Specifically, the conversion was maintained at 59% (Table S3, see the ESI†), while 88% conversion was observed in the presence of **Ru@rGO/pyr-IMes$_{0.5}$** (Fig. 5c). In addition, the ICP analysis after the thermal filtration did not show any metal leaching (see the Experimental section), confirming the heterogeneity of the catalyst.

Conclusions

The catalytic properties of graphene-supported Ru NPs were finely tuned by modifying their metal surface with pyrene-tagged NHC ligands. A combined study comprising EA and BET surface area analysis allowed us to determine the precise amount of pyr-IMes incorporated into the different functionalized catalysts. CO chemisorption studies confirmed both the coordination of NHC ligands to the ruthenium surface and the presence of free Ru sites on these functionalized catalysts. Ligand-stabilized Ru NPs were used as model catalysts for surface studies. The results suggested the presence of a second coordination sphere of pyr-IMes ligands on these non-supported Ru NPs, probably formed by π–π stacking interactions between the aromatic groups of the pyrene-tagged NHCs. Despite the high surface coverage of these non-supported Ru NPs, they still have a large number of available active sites, as was confirmed by DRIFT and solid-state NMR analyses using CO as a molecular probe. Interestingly, by XPS we were able to distinguish the different nature and interaction modes of pyr-IMes ligands on the functionalized catalysts. For example, in **Ru@rGO/pyr-IMes$_{0.5}$**, the pyrene-tagged NHC can be found in three different ways: (i) as a protonated carbene, (ii) coordinated to the ruthenium surface and (iii) directly interacting with the graphene support. According to the catalytic results, we observed that both the activity and selectivity of these graphene-supported Ru NPs were highly dependent on the surface coverage degree. This clear correlation was investigated using acetophenone hydrogenation as a model reaction. The higher the amount of surface NHC ligands, the lower the activity of the catalyst, but the higher the selectivity towards 1-phenylethanol. Moreover, at higher surface coverages the hydrodeoxygenation side-reaction is practically suppressed. This increase in the selectivity at the expense of the activity is explained by the blockage of metal active sites by surface ligands. The reactivity of **Ru@rGO/pyr-IMes$_{0.5}$**, which displays the best balance between activity and selectivity, was also evaluated in the hydrogenation of other substrates of interest, such as 1-methylindole or HMF, among others. Finally, the stability of the modified and non-modified catalysts was studied by TEM analysis after catalysis, observing an evident correlation between the nanoparticle surface ligand coverage and the stability of the supported Ru NPs against sintering. The presence of the pyrene tag on the NHC used as a modifier is crucial to control both the selectivity and stability of these ligand-functionalized supported Ru NPs. In addition, **Ru@rGO/pyr-IMes$_{0.5}$** was employed in multi-addition and "hot filtration" experiments, showing high stability and recyclability. To sum up, these results prove that it is possible to control the activity, selectivity and stability of graphene-supported Ru NPs by modifying their metal surface with organic molecules, making them potential catalysts for industrial applications, since they unify the benefits of homogeneous (high selectivity) and heterogeneous (stability and recyclability) catalysts.

Experimental

General methods

Most chemical operations performed in this work were carried out using conventional Fischer–Porter techniques, Schlenk tubes and a glovebox under a nitrogen atmosphere. Solvents were purified before use, THF (Sigma-Aldrich) by distillation under an argon atmosphere through filtration in the column of a solvent purification system (SPS). The organometallic ruthenium precursor, (1,5-cyclooctadiene)(1,3,5-cyclooctatriene) ruthenium(0) [Ru(COD)(COT)], was purchased from Nanomeps (Toulouse), rGO from Graphenea and acetophenone (99%), decanal (98%), nitrobenzene (99%), styrene (99%), 3-methyl-2-cyclohexenone (98%), quinoline (98%), 1-methylindole (>97%), dodecane (99%) and 1,3-dicyclohexylimidazolium chloride from Merck. All reagents were used without prior purification, except for HMF (97%, Carbosynth) which was purified by filtering with an equimolar silica : alumina mixture, and stored in a refrigerator.

Transmission electron microscopy (TEM) and high-resolution transmission electron microscopy (HRTEM). Non-supported and supported Ru NPs were analyzed by TEM and HRTEM. For the sample preparation, a small amount of the isolated materials was adequately dispersed in THF, and an aliquot was deposited on a copper grid. TEM and HRTEM analyses were performed at the "Servicio de Microscopia Electrónica" of Universitat Politècnica de València (UPV). HRTEM analysis was carried out with a JEOL JEM 2010 electron microscope with a working voltage of 200 kV with a resolution point of 2.35 Å. FFT (fast Fourier transform) treatments were carried out with the DigitalMicrograph program version 3.7.4. TEM observation was performed by using a JEOL JEM 1400Flash electron microscope operating at 120 kV with a point resolution of 3.8 Å. The measurement of the size distribution of the nanoparticles was performed with the ImageJ program by analyzing their length on a given area of the copper grid.

Elemental analysis (EA). Measurements were carried out on a Euro EA3000 elemental analyzer (EuroVector), using sulfanilamide as a reference standard.

Gas chromatography (GC). The spectra of the reactants and their hydrogenated products were recorded with an Agilent Technologies 7890A GC-system with a flame ionization detector and a HP-5 column. The method used started with the injection temperature T0. After holding this temperature for 2 min, the column was heated to temperature T1 (10 °C min^{-1}) and finally, the column was heated to T2 (30 °C min^{-1}) which was held for 1 min (T0 = 80 °C, T1 = 160 °C, T2 = 280 °C). On the other hand, the spectra of HMF and derivatives were obtained with Varian CP-3800 equipment with a Varian CP-8400 automatic injector and a Carbowax column. The method used started with an injection temperature of 50 °C. After holding this temperature for 1 minute, the column was heated to 240 °C (20 °C min^{-1}) and this temperature was maintained for 3.5 minutes. Dodecane was used as an internal standard.

Gas chromatography-mass spectrometry (GC-MS). GC-MS analyses were carried out on an Agilent 6890N chromatograph equipped with a HP-5 column (30 m, 0.32 mm, 0.25 μm), coupled to an Agilent 5973N electron impact mass spectrometer.

Inductively coupled plasma optical emission spectrometry (ICP-OES). Digestion of the graphene supported Ru NPs was performed in a microwave oven for an hour by adding a 3 : 1 solution of nitric and hydrochloric acid over 12 h. The ICP analysis was performed with an Agilent 7500 CX. The metal content of the ligand stabilized Ru NPs (**Ru/pyr-IMes$_{0.2}$** and **Ru/pyr-IMes$_{0.5}$**) was measured by Kolbe MikroLab by ICP-AES.

Raman spectroscopy. For the measurement of the Raman spectra, excitation wavelengths of 514 and/or 785 nm were set for a Renishaw inVia Raman spectrometer equipped with a Leica microscope. The samples (powder) were deposited in an aluminum support and measured within the region of 0 to 3000 cm^{-1} with a resolution of <4 cm^{-1}.

X-ray photoelectron spectroscopy (XPS). XPS analyses were performed using a SPECS device equipped with a Phoibos 150-9MCD detector using Mg-Kα radiation ($h\nu$ = 1235.6 eV) and Al-Kα radiation ($h\nu$ = 1483.6 eV) from a dual source. During the measurements, the pressure was maintained below 10^{-9} Torr. The quantification and evaluation of the spectra were carried out with the help of the CASA software, using C 1s = 284.5 eV as a reference.

Solid-state magic angle spinning nuclear magnetic resonance (MAS-NMR) spectroscopy. MAS-NMR analyses with and without ^{1}H–^{13}C cross-polarization (CP) were performed at the ITQ on a Bruker Avance 400WB instrument equipped with a 3.2 mm probe and with a sample rotation frequency of 10 kHz. Measurements were made using a 3.2 mm ZrO_2 rotor.

Chemisorption. CO adsorption measurements were taken using the double isotherm method on a Quantachrome Autosorb-1C equipment. Prior to adsorption, the samples were reduced *in situ* in flowing pure hydrogen (25 mL min^{-1}) at 200 °C for 3 h (10 °C min^{-1} rate). After reduction, the samples were degassed at 1333 × 10^{-3} Pa for 2 h at the reduction temperature, and then the temperature was lowered to 25 °C (1 hour for cooling down the sample to adsorption temperature). Then, pure CO was introduced and the first adsorption isotherm (*i.e.* the total CO uptake) was measured. After evacuation at 25 °C, the second isotherm (*i.e.* the reversible CO uptake) was taken. The amount of chemisorbed CO was then obtained by subtracting the two isotherms. The pressure range studied was 0.5–11 × 10^4 Pa.

BET. The isotherms were recorded with a Micrometrics ASAP-2000 at a temperature of −196 °C. The samples were vacuum treated for 24 hours before adsorption measurements that were carried out at a temperature of 120 °C.

Diffuse reflectance infrared Fourier transform (DRIFT) spectroscopy. DRIFT measurements were taken on a Bruker Vertex 70 equipment with a 3 mm aperture, 20 kHz speed and a resolution of 4 cm^{-1}. The samples were prepared by dropping a drop of a THF solution of the ligand (**pyr-IMes**) or the colloidal nanoparticles (**Ru/pyr-IMes**), before and after bubbling CO for 5 min, on a well with KBr, which was placed in the cell.

Synthesis of pyr-IMes·HBr

The synthesis of the imidazolium salt (pyr-IMes·HBr) was achieved by following a synthetic method previously described elsewhere.[32]

Synthesis of graphene-supported Ru NPs

Ru@rGO. A Schlenk flask was charged with 10 mg (0.032 mmol) of Ru(COD)(COT) which was dissolved in 3 mL of anhydrous and deoxygenated THF. After that, the solution was added to a 250 mL Fischer–Porter bottle with a 100 mg suspension of reduced graphene oxide (rGO) in 50 mL of THF previously sonicated for 90 min. The Fischer–Porter bottle was then pressurized with 3 bar H_2 and the dispersion was stirred vigorously for 20 h at room temperature. After that, the pressure was released and **Ru@rGO** was filtered through a polyamide membrane (Whatman® membrane filters, 47mm × 0.45 μm) under vacuum and washed with 100 mL of THF. Finally, the catalyst was dried in an oven overnight at 60 °C. The mean particle size value obtained for **Ru@rGO** was 1.5 ± 0.5 nm. The ICP measurements showed that the catalyst contained 2.45 wt% of metal.

Ru@rGO/pyr-IMes$_{0.2}$. A Schlenk flask was charged with 10 mg (0.032 mmol) of Ru(COD)(COT) which was dissolved in 3 mL of anhydrous and deoxygenated THF. After that, the solution was added to a 250 mL Fischer–Porter bottle with a

100 mg suspension of reduced graphene oxide (rGO) in 50 mL of THF previously sonicated for 90 min. The Fischer–Porter bottle was then pressurized with 3 bar H_2 and the dispersion was stirred vigorously for 20 h at room temperature. At the same time, a Schlenk flask was charged with pyr-IMes·HBr (3.1 mg, 0.0063 mmol, 0.2 equiv.) and potassium *tert*-butoxide (0.9 mg, 0.0079 mmol, 0.25 equiv.) which were dissolved in 5 mL of deoxygenated and dehydrated THF from the SPS. After 20 h stirring at room temperature, the resulting suspension was filtered through dry Celite (1 cm) under an argon atmosphere and transferred to the Fischer–Porter bottle charged with **Ru@rGO** (where hydrogen pressure was released previously). The stirring was kept for 1 h, and the resulting solid was filtered through a polyamide membrane (Whatman® membrane filters, 47mm × 0.45 μm) under vacuum and washed with 100 mL of THF. Finally, the black precipitate was dried overnight in an oven at 60 °C. The nanoparticle size was measured by TEM on a population of at least 100 NPs, which afforded a mean value of 1.5 ± 0.4 nm. The ICP measurements showed that the catalyst contained 2.43 wt% of metal.

Ru@rGO/pyr-IMes$_{0.5}$. For this synthesis, the procedure described for **Ru@rGO/pyr-IMes$_{0.2}$** has been followed, but adding 7.6 mg (0.0159 mmol, 0.5 equiv.) of pyr-IMes·HBr and 2 mg (0.0174 mmol, 0.55 equiv.) of K^{t}BuO instead. The mean particle size value obtained was 1.5 ± 0.3 nm. The ICP measurements showed that the catalyst contained 2.48 wt% of metal.

Ru@rGO/pyr-IMes$_{0.8}$. For this synthesis, the procedure described for **Ru@rGO/pyr-IMes$_{0.2}$** has been followed, but adding 12.2 mg (0.0253 mmol, 0.8 equiv.) of pyr-IMes·HBr and 3 mg (0.0270 mmol, 0.88 equiv.) of K^{t}BuO instead. The mean particle size value was 1.6 ± 0.7 nm. The ICP measurements showed that the catalyst contained 2.50 wt% of metal.

Ru@rGO/pyr-IMes$_1$. For this synthesis, the procedure described in **Ru@rGO/pyr-IMes$_{0.2}$** has been followed, but adding 15.3 mg (0.0317 mmol, 1 equiv.) of pyr-IMes·HBr and 3.7 mg (0.0333 mmol, 1.1 equiv.) of K^{t}BuO instead. The mean particle size value obtained was 1.6 ± 0.4 nm. The ICP measurements showed that the catalyst contained 2.32 wt% of metal.

Ru@rGO/ICy$_1$. For this synthesis, the procedure described in **Ru@rGO/pyr-IMes$_{0.2}$** has been followed, but adding 8.5 mg (0.0317 mmol, 1 equiv.) of ICy·HCl and 3.7 mg (0.0333 mmol, 1.1 equiv.) of K^{t}BuO instead. The mean particle size value obtained was 1.6 ± 0.5 nm.

Synthesis of ligand-stabilized Ru NPs

Ru/pyr-IMes$_{0.2}$. A Schlenk flask was charged with pyr-IMes·HBr (30.5 mg, 0.0634 mmol, 0.2 equiv.) and K^{t}BuO (10 mg, 0.0793 mmol, 0.25 equiv.) which were dissolved in 10 mL of deoxygenated and dehydrated THF from the SPS. After that the solution was added to a 250 mL Fischer–Porter bottle charged with a cooled solution (−80 °C) of Ru(COD)(COT) (100 mg, 0.32 mmol) in 50 mL of THF (previously degassed by three freeze–pump cycles). The Fischer–Porter bottle was then pressurized with 3 bar H_2, and the solution was allowed to reach room temperature while the solution was stirred vigorously. A black homogeneous solution was immediately formed, and the stirring was kept for 20 hours at room temperature. After that, the remaining H_2 pressure was released with vacuum, and 50 mL of anhydrous pentane was added to the solution to favour the precipitation of **Ru/pyr-IMes$_{0.2}$** NPs, and then they were dried overnight under vacuum. The size of the NPs was measured by TEM on a sample of a least 100 nanoparticles, which afforded a mean value of 1.4 ± 0.4 nm. ICP gave the following Ru content: 55.7%.

Ru/pyrIMes$_{0.5}$. The same procedure as previously described for **Ru/pyr-IMes$_{0.2}$** has been followed, with the difference that 76.3 mg (0.1585 mmol, 0.5 equiv.) of pyr-IMes·HBr and 25 mg (0.1744 mmol, 0.55 equiv.) of K^{t}BuO were added. The size of the nanoparticles was measured by TEM analyzing a sample which contained at least 100 particles, obtaining an average value of 1.3 ± 0.4 nm. The metallic content has been quantified by ICP, giving an experimental Ru content of 33.2%.

Synthesis of pyr-IMes/rGO

pyr-IMes/rGO. A Schlenk flask was charged with 7.6 mg (0.0159 mmol, 0.5 equiv.) of pyr-IMes·HBr and 2 mg (0.0174 mmol, 0.55 equiv.) of K^{t}BuOH which were dissolved in 5 mL of deoxygenated and dehydrated THF. The solution was stirred vigorously for 20 h at room temperature. After that, a Fischer–Porter bottle was charged with 100 mg of reduced graphene oxide (rGO) which was dissolved in 50 mL of anhydrous and deoxygenated THF. The solution was sonicated for 90 min to ensure its dispersion. Later, the pyr-IMes$_{(0.5)}$ solution was filtered through dry Celite (1 cm) under an argon atmosphere and transferred to the Fischer–Porter bottle charged with rGO. The stirring was kept for 1 h, and the resulting solid was filtered through a polyamide membrane (Whatman® membrane filters, 47mm × 0.45 μm) under vacuum and washed with 100 mL of THF. Finally, the black precipitate was dried overnight in an oven at 60 °C.

Catalytic hydrogenation reactions

The hydrogenation of acetophenone, 1-methylindole, quinoline and HMF was performed in a 25 mL autoclave engineer reactor, equipped with a mechanical stirrer (750 rpm). Hydrogenation reactions were carried out so that the metal–substrate molar ratio was 1 : 200. In this way, considering that 0.5 mmol of substrate was used and each catalyst has 3 wt% of the Ru metal, 0.5 mol% of the metal-catalyst was added in each reaction, which means 0.0025 mmol of metal in each case. For all the immobilized and functionalized catalysts, the exact mass added during the catalysis was 10 mg.

Thus, 10 mg of the catalyst was dispersed in 9 mL of THF and sonicated for 60 minutes. The suspension was transferred into the reactor, which was purged with H_2 three times and finally pressurized with 35 bar H_2. The reactor was then heated at 150 °C, reaching a final pressure of 50 bar. The catalyst was kept under these conditions for one hour, to reduce and activate the active ruthenium species. Before the substrate (0.5 mmol) and dodecane (0.3 mmol) diluted in 1 mL of THF were injected with the help of a 250 μL Hamilton syringe, the temperature was reduced to 130 °C. After maintaining the reaction for 20 h, the reactor temperature was lowered to room temperature and the reactor was depressurized. The resulting suspension was collected, and a fraction was filtered to separate the catalyst from the rest of the solution, which was analyzed by GC and GC-MS.

Kinetic experiments

For the kinetic experiments, the reactor was charged, pressurized and heated under the required conditions, and aliquots were taken from the reaction medium every hour. Then, the aliquot was analyzed by GC using dodecane as the internal standard.

Multi-addition experiments

For the multi-addition experiment, the autoclave was charged, pressurized and heated under the required conditions for acetophenone hydrogenation (130 °C, 50 bar H_2, 10 mL THF). Every 12 hours, an aliquot was taken from the reaction medium and a new starting substrate (*i.e.* acetophenone) was added to the reactor. The aliquots were analyzed by GC using dodecane as the internal standard and confirmed by GC–MS. The activity and selectivity were retained over 7 catalytic cycles confirming the stability of the Ru-NP catalysts.

"Hot filtration" experiment

For the "hot filtration" experiment, the reactor was charged, pressurized and heated under the required conditions for acetophenone hydrogenation (130 °C, 50 bar H_2, 10 ml THF). After 2 h reaction, **Ru@rGO/pyr-IMes$_{0.5}$** was removed by thermal filtration, and another clean and empty autoclave was charged with the mother liquor solution, pressurized and heated under the same reaction conditions. Then, the conversion of acetophenone was determined after 4 h and compared to that at 2 h (Table S2, ESI†). No change in the conversion was observed. After the "hot filtration", the mother liquor solution was analyzed by ICP, with the Ru detected being negligible.

Author contributions

C. C.-N. and A. G.-Z. performed the synthesis and structural/spectroscopic characterization and catalytic experiments and participated in writing – review and editing. A. M.-C. performed the synthesis and spectroscopic characterization of the NHC ligands. P. O.-B., A. C. and J. M. supervised the project and participated in writing – review and editing. L. M. M.-P. conceived the idea of the project and wrote the original draft with input from the other authors. All authors contributed to the design of the experiments, analysis of the results and preparation of the manuscript.

Conflicts of interest

There are no conflicts to declare.

Acknowledgements

The authors thank Instituto de Tecnología Química (ITQ), Consejo Superior de Investigaciones Científicas (CSIC), Universitat Politècnica de València (UPV) and 'Servei Central d'Instrumentació Científica (SCIC) de la Universitat Jaume I' for the facilities and MICIU/AEI/FEDER (RTI2018-098237-B-C22) and Universitat Jaume I (UJI-B2018-23) for the financial support. We also thank the Electron Microscopy Service of the UPV for the TEM facilities, Jose A. Vidal-Moya (ITQ, CSIC-UPV) for the MAS-NMR measurements and J. Gaona for his assistance with the catalytic reactions. A. G.-Z. acknowledges "Programa de Ayudas del Aula Cemex Sostenibilidad" for the completion of the Master's Thesis in Sustainable Chemistry and C. C.-N. gratefully thanks the Generalitat Valenciana predoctoral fellowship (GVA: ACIF/2019/076). A. M.-C. thanks Generalitat Valenciana for a grant (ACIF/2019/100).

Notes and references

1 (*a*) D. Astruc, *Chem. Rev.*, 2020, **120**, 461; (*b*) P. Serp and K. Philippot, *Nanomaterials in Catalysis*, Wiley-VCH, Weinheim, Germany, 2013; (*c*) D. Astruc, *Nanoparticles and Catalysis*, Wiley-VCH, Weinheim, Germany, 2008.

2 D. Astruc, F. Lu and J. R. Aranzaes, *Angew. Chem., Int. Ed.*, 2005, **44**, 7852.

3 (*a*) M. R. Axet and K. Philippot, *Nanoparticles in Catalysis: Advances in Synthesis and Applications*, Wiley-VCH, Weinheim, Germany, 2021; (*b*) L. M. Martínez-Prieto and P. W. N. M. van Leeuwen, *Ligand effects in ruthenium nanoparticle catalysis*, 2020, pp. 407–448.

4 M. R. Axet and K. Philippot, *Chem. Rev.*, 2020, **120**, 1085.

5 (*a*) C. A. Schoenbaum, D. K. Schwartz and J. W. Medlin, *Acc. Chem. Res.*, 2014, **47**, 1438; (*b*) S. Kunz, *Top. Catal.*, 2016, **59**, 1671.

6 (*a*) K. R. Kahsar, D. K. Schwartz and J. W. Medlin, *J. Am. Chem. Soc.*, 2014, **136**, 520; (*b*) I. Schrader, S. Neumann, A. Šulce, F. Schmidt, V. Azov and S. Kunz, *ACS Catal.*, 2017, **7**, 3979; (*c*) P. D. Coan, L. D. Ellis, M. B. Griffin, D. K. Schwartz and J. W. Medlin, *J. Phys. Chem. C*, 2018, **122**, 6637; (*d*) A. Šulce, J. Backenköhler, I. Schrader, M. D. Piane, C. Müller, A. Wark, L. C. Ciacchi, V. Azov and S. Kunz, *Catal. Sci. Technol.*, 2018, **8**, 6062; (*e*) P. D. Coan, C. A. Farberow, M. B. Griffin and J. W. Medlin, *ACS Catal.*, 2021, **11**, 3730.

7 (*a*) M. J. Climent, A. Corma and S. Iborra, *Chem. Rev.*, 2011, **111**, 1072; (*b*) A. Corma and H. Garcia, *Top. Catal.*, 2008, **48**, 8.

8 Q. L. Zhu and Q. Xu, *Chem*, 2016, **1**, 220.

9 (*a*) Y.-Z. Chen, G. Cai, Y. Wang, Q. Xu, S.-H. Yu and H.-L. Jiang, *Green Chem.*, 2016, **18**, 1212; (*b*) A. Noujima, T. Mitsudome, T. Mizugaki, K. Jitsukawa and K. Kaneda, *Angew. Chem., Int. Ed.*, 2011, **50**, 2986.

10 S. Navalon, A. Dhakshinamoorthy, M. Alvaro and H. Garcia, *Coord. Chem. Rev.*, 2016, **312**, 99.

11 J. Lee, K. S. Novoselov and H. S. Shin, *ACS Nano*, 2011, **5**, 608.

12 (*a*) E. D. Grayfer, L. S. Kibis, A. I. Stadnichenko, O. Y. Vilkov, A. I. Boronin, E. M. Slavinskaya, O. A. Stonkus and V. E. Fedorov, *Carbon*, 2015, **89**, 290; (*b*) D. E. García-Rodríguez, L. H. Mendoza-Huizar and C. Díaz, *Appl. Surf. Sci.*, 2017, **412**, 146; (*c*) I. Fampiou and A. Ramasubramaniam, *J. Phys. Chem. C*, 2012, **116**, 6543.

13 A. J. Arduengo III, R. L. Harlow and M. Kline, *J. Am. Chem. Soc.*, 1991, **113**, 361.

14 (*a*) W. A. Herrmann, J. GoobenL and M. Spiegler, *J. Organomet. Chem.*, 1997, **547**, 357; (*b*) M. Poyatos, J. A. Mata and E. Peris, *Chem. Rev.*, 2009, **109**, 3677; (*c*) L. A. Schaper, S. J. Hock, W. A. Herrmann and F. E. Kühn, *Angew. Chem., Int. Ed.*, 2012, **52**, 270.

15 M. N. Hopkinson, C. Richter, M. Schedler and F. Glorius, *Nature*, 2014, **510**, 485.

16 (*a*) M. Koy, P. Bellotti, M. Das and F. Glorius, *Nat. Catal.*, 2021, **4**, 352; (*b*) C. A. Smith, M. R. Narouz, P. A. Lummis, I. Singh, A. Nazemi, C. H. Li and C. M. Crudden, *Chem. Rev.*, 2019, **119**, 4986; (*c*) C. Cerezo-Navarrete, P. Lara and L. M. Martínez-Prieto, *Catalysts*, 2020, **10**, 1144.

17 E. C. Hurst, K. Wilson, I. J. S. Fairlamb and V. Chechik, *New J. Chem.*, 2009, **33**, 1837.

18 U. Hintermair, S. M. Hashmi, M. Elimelech and R. H. Crabtree, *J. Am. Chem. Soc.*, 2012, **134**, 9785.

19 (*a*) P. Lara, O. Rivada-Wheelaghan, S. Conejero, R. Poteau, K. Philippot and B. Chaudret, *Angew. Chem., Int. Ed.*, 2011, **50**, 12080; (*b*) L. M. Martínez-Prieto, E. A. Baquero, G. Pieters, J. C. Flores, E. De Jesús, C. Nayral, F. Delpech, P. W. N. M. Van Leeuwen, G. Lippens and B. Chaudret, *Chem. Commun.*, 2017, **53**, 5850.

20 M. D. de los Bernardos, S. Perez-Rodriguez, A. Gual, C. Claver and C. Godard, *Chem. Commun.*, 2017, **53**, 7894.

21 K. V. S. Ranganath, J. Kloesges, A. H. Schäfer and F. Glorius, *Angew. Chem., Int. Ed.*, 2010, **49**, 7786.

22 (*a*) E. A. Baquero, S. Tricard, J. C. Flores, E. de Jesús and B. Chaudret, *Am. Ethnol.*, 2014, **126**, 13436; (*b*) E. A. Baquero, S. Tricard, Y. Coppel, J. C. Flores, B. Chaudret and E. De Jesús, *Dalton Trans.*, 2018, **47**, 4093.

23 (*a*) C. Richter, K. Schaepe, F. Glorius and B. J. Ravoo, *Chem. Commun.*, 2014, **50**, 3204; (*b*) L. M. Martínez-Prieto, A. Ferry, P. Lara, C. Richter, K. Philippot, F. Glorius and B. Chaudret, *Chem. – Eur. J.*, 2015, **21**, 17495; (*c*) L. M. Martinez-Prieto, A. Ferry, L. Rakers, C. Richter, P. Lecante, K. Philippot, B. Chaudret and F. Glorius, *Chem. Commun.*, 2016, **52**, 4768.

24 (*a*) L. M. Martínez-Prieto, L. Rakers, A. M. López-Vinasco, I. Cano, Y. Coppel, K. Philippot, F. Glorius, B. Chaudret and P. W. N. M. van Leeuwen, *Chem. – Eur. J.*, 2017, **23**, 12779; (*b*) L. C. Moraes, R. C. Figueiredo, J. P. Espinós, F. Vattier, A. Franconetti, C. Jaime, B. Lacroix, J. Rojo, P. Lara and S. Conejero, *Nanoscale*, 2020, **12**, 6821.

25 (*a*) C. Taglang, L. M. Martínez-Prieto, I. del Rosal, L. Maron, R. Poteau, K. Philippot, B. Chaudret, S. Perato, A. Sam Lone, C. Puente, C. Dugave, B. Rousseau and G. Pieters, *Angew. Chem.*, 2015, **127**, 10620; (*b*) A. Palazzolo, S. Feuillastre, V. Pfeifer, S. Garcia-Argote, D. Bouzouita, S. Tricard, C. Chollet, E. Marcon, D.-A. Buisson, S. Cholet, F. Fenaille, G. Lippens, B. Chaudret and G. Pieters, *Angew. Chem., Int. Ed.*, 2019, **58**, 4891.

26 (*a*) D. Gonzalez-Galvez, P. Lara, O. Rivada-Wheelaghan, S. Conejero, B. Chaudret, K. Philippot and P. W. N. M. Van Leeuwen, *Catal. Sci. Technol.*, 2013, **3**, 99; (*b*) P. Lara, A. Suárez, V. Collière, K. Philippot and B. Chaudret, *ChemCatChem*, 2013, **6**, 87; (*c*) M. Axet, S. Conejero and I. C. Gerber, *ACS Appl. Nano Mater.*, 2018, **1**, 5885.

27 (*a*) P. Tegeder, M. Freitag, K. M. Chepiga, S. Muratsugu, N. Möller, S. Lamping, M. Tada, F. Glorius and B. J. Ravoo, *Chem. – Eur. J.*, 2018, **24**, 18682; (*b*) R. Ye, A. V. Zhukhovitskiy, R. V. Kazantsev, S. C. Fakra, B. B. Wickemeyer, F. D. Toste and G. A. Somorjai, *J. Am. Chem. Soc.*, 2018, **140**, 4144.

28 J. B. Ernst, S. Muratsugu, F. Wang, M. Tada and F. Glorius, *J. Am. Chem. Soc.*, 2016, **138**, 10718.

29 A. Palazzolo, T. Naret, M. Daniel-Bertrand, D. Buisson, S. Tricard, P. Lesot, Y. Coppel, B. Chaudret, S. Feuillastre and G. Pieters, *Angew. Chem.*, 2020, **132**, 21065.

30 (*a*) D. Ventura-Espinosa, S. Martín, H. García and J. A. Mata, *J. Catal.*, 2021, **394**, 113; (*b*) D. Ventura-Espinosa, S. Martín and J. A. Mata, *J. Catal.*, 2019, **375**, 419; (*c*) A. Mollar-Cuni, D. Ventura-Espinosa, S. Martín, Á. Mayoral, P. Borja and J. A. Mata, *ACS Omega*, 2018, **3**, 15217.

31 (*a*) L. M. Martínez-Prieto, M. Puche, C. Cerezo-Navarrete and B. Chaudret, *J. Catal.*, 2019, **377**, 429; (*b*) C. Cerezo-Navarrete, Y. Mathieu, M. Puche, C. Morales, P. Concepción, L. M. Martínez-Prieto and A. Corma, *Catal. Sci. Technol.*, 2021, **11**, 494.

32 D. Ventura-Espinosa, S. Sabater and J. A. Mata, *J. Catal.*, 2017, **352**, 498.

33 S. Stankovich, D. A. Dikin, R. D. Piner, K. A. Kohlhaas, A. Kleinhammes, Y. Jia, Y. Wu, S. B. T. Nguyen and R. S. Ruoff, *Carbon*, 2007, **45**, 1558.

34 (*a*) L. M. Martinez-Prieto, I. Cano, A. Marquez, E. A. Baquero, S. Tricard, L. Cusinato, I. del Rosal, R. Poteau, Y. Coppel, K. Philippot, B. Chaudret, J. Campora and P. W. N. M. van Leeuwen, *Chem. Sci.*, 2017, **8**, 2931.

35 L. M. Martinez-Prieto, C. Urbaneja, P. Palma, J. Campora, K. Philippot and B. Chaudret, *Chem. Commun.*, 2015, **51**, 4647.

36 F. Novio, K. Philippot and B. Chaudret, *Catal. Lett.*, 2010, **140**, 1.

37 M. Koy, P. Bellotti, M. Das and F. Glorius, *Nat. Catal.*, 2021, **4**, 352.

38 F. Martinez-Espinar, P. Blondeau, P. Nolis, B. Chaudret, C. Claver, S. Castillón and C. Godard, *J. Catal.*, 2017, **354**, 113.

39 A. Rühling, K. Schaepe, L. Rakers, B. Vonhören, P. Tegeder, B. J. Ravoo and F. Glorius, *Angew. Chem., Int. Ed.*, 2016, **55**, 5856.

40 P. W. N. M. van Leeuwen, *Homogeneous Catalysis-Understanding the Art*, Kluwer Academic Publishers, Netherlands, 2004.

41 (*a*) A. Denicourt-Nowicki, B. Leger and A. Roucoux, *Phys. Chem. Chem. Phys.*, 2011, **13**, 13510; (*b*) D. Duraczynska, A. Drelinkiewicz, E. Bielanska, E. M. Serwicka and L. Litynska-Dobrzynska, *Catal. Lett.*, 2011, **141**, 83.

42 M. Yang, G. Cheng, D. Xie, T. Zhu, Y. Dong, H. Ke and H. Cheng, *Int. J. Hydrogen Energy*, 2018, **43**, 8868.